Elusive Dzyaloshinskii-Moriya interaction in Fe 3 GeTe 2 monolayer

Slimane Laref, Kyoung-Whan Kim, Aurélien Manchon

Elusive Dzyaloshinskii-Moriya interaction in Fe_3GeTe_2 monolayer

Slimane Laref[1],* Kyoung-Whan Kim[2], and Aurélien Manchon[1,3]†
[1] *Physical Science and Engineering Division (PSE), King Abdullah University of Science and Technology (KAUST), Thuwal 23955-6900, Kingdom of Saudi Arabia*
[2] *Center for Spintronics, Korea Institute of Science and Technology, Seoul 02792, Korea*
[3] *Aix Marseille Univ, CNRS, CINAM, Marseille, France.*

Using symmetry analysis and density functional theory calculations, we uncover the nature of Dzyaloshinskii-Moriya interaction in Fe_3GeTe_2 monolayer. We show that while such an interaction might result in small distortions of the magnetic texture on the short range, on the long range Dzyaloshinskii-Moriya interaction favors in-plane Néel spin-spirals along equivalent directions of the crystal structure. Whereas our results show that the observed Néel skyrmions cannot be explained by the Dzyaloshinskii-Moriya interaction at the monolayer level, they suggest that canted magnetic texture shall arise at the boundary of Fe_3GeTe_2 nanoflakes or nanoribbons and, most interestingly, that homochiral planar magnetic textures could be stabilized.

Introduction. Magnetism in low dimensions has received renewed interest in the past few years with the observation of remnant magnetization in two-dimensional van der Waals materials such as CrI_3[1], VTe_2[2], $CrTe_2$[3], and Fe_3GeTe_2[4]. Robust magnetic order at room temperature is appealing for spintronics applications, and among the ever-increasing family of candidate materials Fe_3GeTe_2 stands out as a solid paradigm[4–6]. Indeed, spin-orbit torque[7,8] and anomalous Nernst effect[9,10] have been observed in bilayer heterostructures, and magnetoresistance has been reported in spin-valves[11,12]. Besides these experimental achievements, the recent reports of magnetic skyrmions and other chiral textures in thick Fe_3GeTe_2 layers[13–15] are intriguing.

In fact, stable and metastable chiral magnetic textures require the existence of an antisymmetric exchange interaction, called Dzyaloshinskii-Moriya interaction[16,17] (DMI). This interaction only exists in materials lacking inversion symmetry and its specific structure determines the nature of the chiral magnetic structures it can stabilize[18]. For instance, in magnetic multilayers the interfacial symmetry breaking promotes an interfacial DMI of the form $E_{\rm DM} = D\mathbf{m}\cdot[(\mathbf{z}\times\boldsymbol{\nabla})\times\mathbf{m}]$ that favors Néel skyrmions (e.g., see Ref. 19). Therefore, the observation of Néel-type skyrmions in thick Fe_3GeTe_2 layers[13–15] is unexpected as the point group of Fe_3GeTe_2 monolayer prevents the onset of "interfacial" DMI. Yet, the emergence of chiral effects is not entirely forbidden and Johansen et al.[20] recently showed that Fe_3GeTe_2 monolayer exhibits a dampinglike spin-orbit torque of unusual symmetry. Since DMI and dampinglike torque are related to each other[21], one expects a non-vanishing DMI of completely different nature compared to the interfacial one.

In this work, using symmetry analysis and density functional theory (DFT) calculations, we investigate the nature of DMI in Fe_3GeTe_2 monolayer. We show that while such an interaction might result in small distortions of the magnetic texture on the short range, on the long-wavelength limit DMI favors in-plane Néel spin-spirals along low-symmetry directions of the crystal. Whereas these results show that the observed Néel skyrmions cannot be explained by the DMI at the monolayer level, they suggest that a canted magnetic texture shall arise at the boundary of Fe_3GeTe_2 nanoflakes and that homochiral planar magnetic textures can be stabilized.

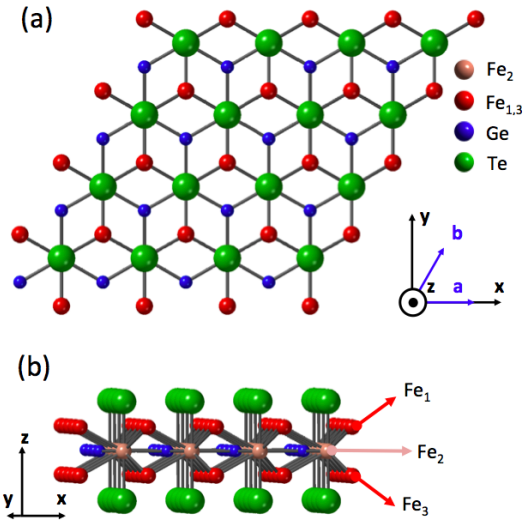

FIG. 1. (Color online) (a) Top and (b) side view of Fe_3GeTe_2 monolayer. (x, y, z) are the cartesian coordinates and ($\mathbf{a}$, $\mathbf{b}$) are the equivalent crystallographic directions.

Long-wavelength behavior. Let us first consider the crystal structure of Fe_3GeTe_2 monolayer, depicted on Fig. 1. The crystal adopts the point group $\bar{6}m2$ and can be seen as a stack of three Fe hexagonal lattices in A-B-A configuration. In the following, the central Fe element is denoted Fe_2 and the Fe elements on the top and bottom planes are referred to as $Fe_{1,3}$, respectively. These three inequivalent Fe elements are located in a chemical environment that lacks inversion symmetry. Therefore, one can expect each magnetic element to experience chiral effects such as DMI and spin-orbit torques in the presence of spin-orbit coupling (SOC). However, Fe_1 and Fe_3 are mirror partners, so any chiral physical quantity on one element is opposite on the other. In contrast, Fe_2 is located in the mirror plane of the crystal and therefore

should experience chiral effects.

A first indication is provided by analyzing the point group of Fe_3GeTe_2 monolayer. Applying these symmetries (improper six-fold rotation about [001], mirror symmetry normal to [110]) to the current-driven field response tensor[22], one obtains an unusual non-zero dampinglike torque[20]

$$\mathbf{T}_{\rm DL} = \eta \mathbf{m} \times [(m_y E_x + m_x E_y)\mathbf{x} + (m_x E_x - m_y E_y)\mathbf{y}]. \tag{1}$$

Here, η is the torque response coefficient and $\mathbf{E}$ is the applied electric field. This torque behaves like a nonequilibrium magnetocrystalline anisotropy term[20] whose influence on the magnetic texture of Fe_3GeTe_2 is left to future studies. One can show that *in the limit of small spatial gradients*, i.e., in the long-wavelength limit, the Dzyaloshinskii-Moriya (DM) tensor has the same symmetry as the dampinglike torque response tensor[21]. Defining the torque response tensor $\hat{\chi}_{\rm DL}$ as $\mathbf{T}_{\rm DL} = \hat{\chi}_{\rm DL} \cdot \mathbf{E}$ and the DM tensor $\hat{D}$ as $E_{\rm DM} = \sum_{ij} D_{ij} \mathbf{e}_i \cdot (\mathbf{m} \times \partial_j \mathbf{m})$, the linear response theory yields $\hat{\chi}_{\rm DL} \propto \hat{D}$. Specifically,

$$\hat{\chi}_{\bar{6}m2} = \eta \begin{pmatrix} -m_z m_x & m_z m_y & 0 \\ m_z m_y & m_z m_x & 0 \\ m_x^2 - m_y^2 & -2 m_y m_x & 0 \end{pmatrix} \propto \hat{D}_{\bar{6}m2}, \tag{2}$$

which leads to the DM energy

$$E_{\rm DM} = D[-\partial_x (m_y m_x) + \frac{1}{2} \partial_y (m_x^2 - m_y^2)]. \tag{3}$$

Since the DM energy is a total derivative, it does not stabilize chiral textures in the long-wavelength limit. However, one could wonder whether this interaction can stabilize magnetic twists at the edges of the magnetic layer, as discussed recently[23–25]. To investigate this possibility, we consider a magnetic ribbon with easy-plane anisotropy and embedded between two boundaries normal to the direction $\mathbf{n}$. The system is translationally invariant along $\mathbf{z} \times \mathbf{n}$ and spatial gradients are only allowed along $\mathbf{n}$, $\boldsymbol{\nabla} = \partial_{x_n} \mathbf{n}$, where x_n is the coordinate along $\mathbf{n}$. In the bulk of the ribbon, the magnetization $\mathbf{m}$ minimizes the energy functional $W = A(\partial_{x_n} \mathbf{m})^2 + K(\mathbf{m} \cdot \mathbf{z})^2$, where A is the exchange stiffness and K the easy plane anisotropy. The general solution is $\mathbf{m} = \cos(a x_n + \phi)\mathbf{n} + \sin(a x_n + \phi)\mathbf{z} \times \mathbf{n}$. The boundary condition reads[24]

$$2A(\mathbf{n} \cdot \boldsymbol{\nabla})\mathbf{m} + \mathbf{m} \times (\boldsymbol{\Gamma}_{\rm D} \times \mathbf{m}) = 0, \tag{4}$$

where $\boldsymbol{\Gamma}_{\rm D}$ is the boundary-induced DM field, defined $\boldsymbol{\Gamma}_{\rm D} = m_i n_j D_{ijk}$, with $E_{\rm DM} = \sum_{ijk} D_{ijk} m_i \partial_j m_k$. Solving Eq. (4) at the positions $x_n = x_1$ and $x_n = x_2$, we obtain the condition

$$\cos 2(a x_{1,2} + \phi) = (2A/D)a, \tag{5}$$

yielding the solution, $\sin(a(x_1+x_2)+2\phi)\sin(a(x_2-x_1)) = 0 \Rightarrow a = n\pi/(x_2 - x_1)$. The energy of this spin spiral is $W = An^2\pi^2/L^2$, which is minimized for $n = 0$. Therefore, the DM energy, Eq. (3), does not favor chiral magnetic textures even in the case of a planar ferromagnet. The present discussion only applies in the long-wavelength limit, though, and does not address the possible existence of short-wavelength magnetic textures.

Structural analysis. Let us now take a different perspective and consider the atomistic DMI between neighboring magnetic moments. The relevant pairs of neighboring moments are displayed on Fig. 2 together with the DM vector $\mathbf{D}$, defined in the atomistic spin limit $E_{\rm DM} = \mathbf{D} \cdot (\mathbf{S}_1 \times \mathbf{S}_2)$. The DM vector is determined by Moriya's rules[17].

We first consider the Fe_1-Fe_3 pair, located on each side of the (001) mirror plane [Fig. 2(a)]. Moriya's 1st rule states that the DM vector must lie in the (001) mirror plane, whereas Moriya's 5th rule states that the DM vector is necessarily along the axis of three-fold rotational symmetry. Combining both conditions, DMI necessarily vanishes. Let us now consider the interaction between two Fe_1 (or, equivalently, two Fe_3) belonging to the same layer [Fig. 2(b)]. Since a mirror plane passes perpendicularly through the center of the Fe_1-Fe_1 segment, the DM vector lies in this plane (Moriya's 1st rule). Considering the three-fold rotational symmetry around [001], the DM vector is necessarily along z (5th rule). Notice that the DM vector also possesses an in-plane component that has three-fold symmetry. Moving on to the Fe_1-Fe_2 pair [Fig. 2(c)], the same symmetry principles apply and we find that the DM vector must be perpendicular to the Fe_1-Fe_2 segment. Notice that in the case of the Fe_3-Fe_2 pair, the DM vector adopts the opposite orientation. Finally, the interaction between Fe_2-Fe_2 [Fig. 2(d)] is similar to the one obtained for Fe_1-Fe_1 so that the DM vector possesses a constant z component and a staggered planar component. Notice that the DMIs involving either Fe_1 or Fe_3 are systematically opposite to each other because of the (001) mirror plane. Therefore, one might expect small magnetization canting at the level of the unit cell that could explain the topological Hall effect reported in Ref. 26. However, no overall effect on the long range is expected, consistently with the absence of long-wavelength interaction emphasized above.

What is particularly interesting is that whereas the in-plane component of the DM vector is staggered, the perpendicular (z) component of the Fe_2 layer remains constant over the unit cell. Therefore, one expects that at intermediate range (i.e., beyond the size of a unit cell), the atomistic DM energy reads $E_{\rm DM} = D\mathbf{z} \cdot (\mathbf{S}_1 \times \mathbf{S}_2)$. This interaction is carried by the central Fe elements and its magnitude is therefore associated with the electrostatic environment of Fe_2. This is an important remark because the only heavy element of the structure is Te, which is located further away from Fe_2. Therefore, one expects the overall DMI magnitude to remain small.

Spin spiral calculations. To confirm the analysis provided above, we performed DFT calculations on Fe_3GeTe_2. We used the full-potential linearized augmented-plane-wave (FLAPW) method as imple-

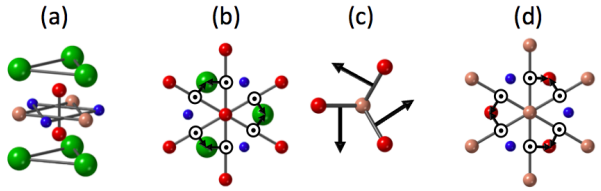

FIG. 2. (Color online) DM vector (black arrows) for various nearest neighbor interactions: (a) Fe_1-Fe_3, (b) Fe_1-Fe_2, (c) Fe_1-Fe_1 and (d) Fe_2-Fe_2. The chemical elements are designated by the same color code as in Fig. 1. In these figures, we only represented the atoms that contribute to defining the local symmetry of the environment and removed the other elements for better clarity.

Element	Spin moment	Orbital moment
$Te_{1,2}$	-0.024	-0.02
$Fe_{1,3}$	2.267	0.083
Fe_2	1.287	0.19
Ge	-0.06	0.0065

TABLE I. Spin and orbital moments of the various elements (in units of μ_B).

mented in FLEUR software[27]. Applying the generalized Bloch theorem[28], we first self-consistently compute the total energy of the system for spin spirals with different wavelengths q including the scalar-relativistic effects but in the absence of SOC, $\epsilon^{\mathrm{SR}}(q)$. Then, we turn on SOC and compute the spin spiral dispersion at the first order only, $\epsilon^{\mathrm{SOC}}(q)$. The scalar-relativistic dispersion $\epsilon^{\mathrm{SR}}(q)$ provides the exchange stiffness A, while the difference $\epsilon^{\mathrm{SOC}}(q) - \epsilon^{\mathrm{SR}}(q)$ provides a measure of the magnetic anisotropy K (at q=0) and DM coefficient D[29–31]. For the structural relaxation, we employed the generalized gradient approximation (GGA)[32], obtaining a relaxed lattice constant of 4.01 Å for Fe_3GeTe_2 monolayer. For the magnetic calculations, we used the local density approximation (LDA)[33]. In all calculations, we selected the radii of muffi-tin spheres around 2.1 a.u for Ge and Fe, and 2.6 a.u for Te, where a.u is the Bohr radius. The FLAPW basis functions included all wave vectors up to $k_{max} = 3.8$ a.u^{-1} in the interstitial region and in the muffin-tin spheres, and basis functions including spherical harmonics up to $l_{max} = 8$ were taken into account. Collinear (non-collinear + SOC) calculations were performed on a dense mesh of 512 (1024) k-points in the full two-dimensional Brillouin zone.

Based on this procedure, we obtain the spin- and orbital-resolved magnetic moments displayed in Table I and a perpendicular magnetic anisotropy (PMA) K=1.3 meV/Fe. We have performed spin spiral dispersion calculation for three standard configurations[34] - Néel out-of-plane, Bloch out-of-plane and Néel in-plane - and found

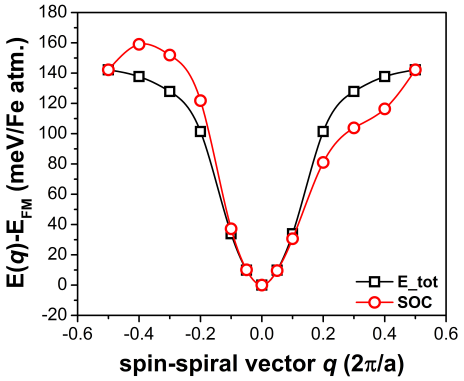

FIG. 3. (Color online) Spin spiral dispersion for Néel in-plane along ΓK without (black) and with (red) SOC. The antisymmetric distortion upon turning on SOC is attributed to DMI. The vertical shift due to magnetic anisotropy has been removed manually for clarity, and the exchange stiffness is A=47 meV/Fe.

that only the latter displays DMI, consistently with the previous analysis. In addition, DMI only exists along ΓK (see Fig. 3) and vanishes along ΓM (not shown). Indeed, the former corresponds to a direction of mirror symmetry *breaking* in real space, whereas the latter corresponds to a direction of mirror symmetry, as illustrated on Fig. 4. Since DMI arises from the interference of Bloch electrons following clockwise and counterclockwise paths, it vanishes along ΓM due to the symmetric chemical environment (green arrows) and is finite along ΓK due to the symmetry breaking (red and blue arrows).

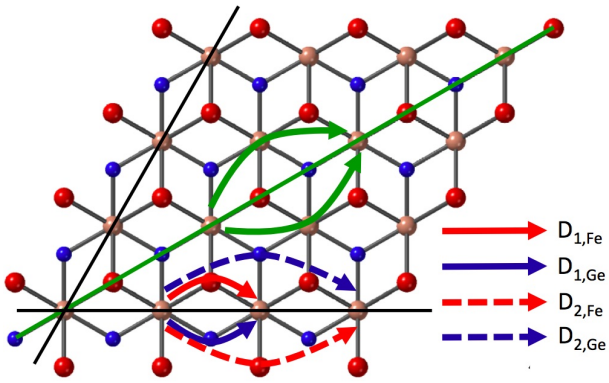

FIG. 4. (Color online) The mirror symmetry normal to the (110) plane (green line) results in a vanishing DM vector along ΓM, whereas the mirror symmetry breaking normal to the (100) plane (black lines) leads to uncompensated clockwise and anticlockwise paths (rounded arrows) and a finite DM vector along ΓK. $D_{i,\alpha}$ denotes the path connecting ith nearest-neighbor Fe_2 sites passing through element α.

To understand the microscopic origin of the perpendicular DMI, Fig. 5 displays the contribution of the various chemical elements on the antisymmetric spin spiral

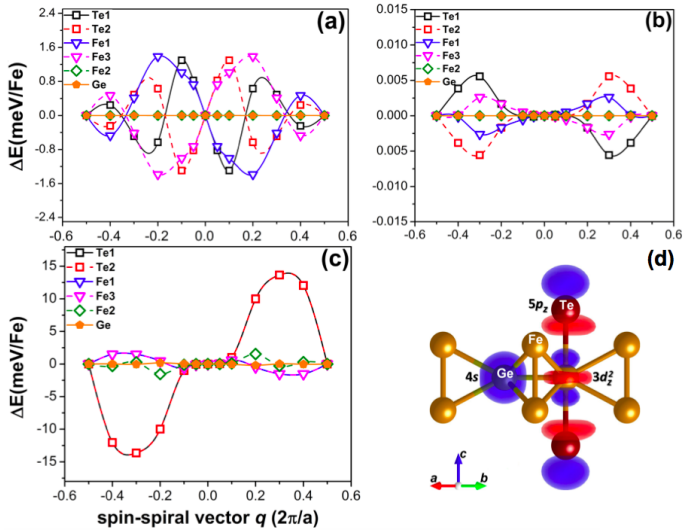

FIG. 5. (Color online) Contribution of the different elements to the antisymmetric part of the spin spiral dispersion along ΓK for (a) Néel out-of-plane, (b) Bloch out-of-plane and (c) Néel in-plane configurations. (d) Kohn-Sham orbitals at Γ-point showing the strong Te $5p_z$-Fe_2 $3d_{z^2}$ hybridization responsible for the large perpendicular orbital moment on Fe_2.

dispersion for the three configurations. For Néel out-of-plane spin spiral [Fig. 5(a)], the main contributions come from top and bottom $Fe_{1,3}$ and Te elements. They are sizable in magnitude but cancel each other by symmetry. For Bloch out-of-plane spin spiral [Fig. 5(b)], we obtain the same cancellation by symmetry but the magnitude of the individual contributions remain extremely small (a few μeV/Fe), below the accuracy of our calculations. Finally, for Néel in-plane spin spiral [Fig. 5(c)], the antisymmetric dispersion is dominated by the hybridization between the $5p_z$ orbitals of Te and the $3d_{z^2}$ orbitals of the central Fe_2 element [see Fig. 5(d)]. It induces a large orbital momentum on Fe_2 ($0.19\mu_B$), as displayed in Table I, that is responsible for the observed DMI. In contrast, the $Fe_{1,3}$ elements hardly contribute because of their weak orbital moment ($0.083\mu_B$).

We complete this analysis by discussing the potential influence of the perpendicular DMI of the stabilization of magnetic textures. It is clear that the large PMA of Fe_3GeTe_2 hinders the stabilization of Néel in-plane spin spirals. Nevertheless, for the sake of the discussion let us disregard the role of the magnetic anisotropy and only focus on the influence of the DMI itself. Intriguingly, the antisymmetric dispersion [Fig. 5(c)] is quite different from the dispersion obtained at, e.g., transition metal interfaces[30,31,35]. In the latter, the antisymmetric contribution of the dispersion has a large slope around $q = 0$, from which the long-wavelength DM coefficient is usually extracted. In Fig. 5(c), the slope close to $q = 0$ vanishes and the antisymmetric dispersion only takes off away from the origin. Qualitatively, this quenching is associated to a partial compensation of the high-order DM coefficients, as illustrated on Fig. 4. For nearest neighbor DMI, electrons following clockwise (red solid arrow) and anticlockwise paths (blue solid arrow) pass either through $Fe_{1,3}$ ($D_{1,Fe}$) or through Ge ($D_{1,Ge}$), respectively. For next-nearest neighbor DMI though, the chemical environment is partly inverted as the clockwise path (blue dashed arrow) passes through Ge ($D_{2,Ge}$), whereas the anticlockwise path (red dashed arrow) passes through $Fe_{1,3}$ ($D_{2,Fe}$). As a result, the next-nearest neighbor DM vector partially compensates the nearest neighbor DM vector. By generalizing this reasoning to higher-order DM coefficients (beyond the next-nearest neighbor), one expects that the DM energy is quenched close to $q = 0$.

This feature means that the DMI has no impact in the long wavelength limit and is unlikely to stabilize large (>10 nm) chiral textures. Nonetheless, it does tend to stabilize short-wavelength spin spirals. Indeed, the dispersion is peaked around $q \approx \frac{\pi}{\sqrt{3}a}$. Considering that this dispersion is computed along the ΓK path, it means that DMI tends to stabilize planar homochiral spin spirals propagating along a low symmetry direction of the Fe_3GeTe_2 crystal. Figure 6 shows such a planar spin spiral extended along the [100] direction of the crystal (dashed lines), characterized by broken mirror symmetry.

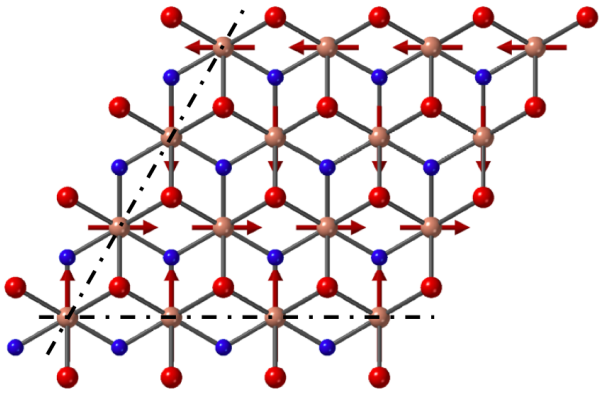

FIG. 6. (Color online) Example of a planar homochiral spin spiral propagating along the low symmetry [100] direction (dashed line), characterized by mirror symmetry breaking.

Conclusion. Using symmetry arguments and DFT calculations, we have shown that the DMI of Fe_3GeTe_2 adopts the form $D\mathbf{z}\cdot(\mathbf{S}_1\times\mathbf{S}_2)$, with a DM vector normal to the (001) plane. This interaction is unable to stabilize the Néel skyrmions reported recently in thick Fe_3GeTe_2 layers, but it possesses remarkable characteristics. It vanishes in the long wavelength limit and only survives for small textures as it tends to stabilize planar spin spirals with wave vector $q \approx \frac{\pi}{\sqrt{3}a}$ and propagating along ΓK direction. Nonetheless, in realistic situations, the large PMA of Fe_3GeTe_2 monolayers prevents the formation of such planar spin spirals, at least in the monolayer limit. Cancelling this PMA by surface engineering represents an appealing challenge as it could open avenues

for the generation of unusual chiral textures. In fact, since magnetic anisotropy is driven by tiny details of the band structure[36] (from μeV to meV), it is highly sensitive to the band filling and can be tuned easily by doping[6], Fe-Co alloying[37] or using a gate voltage[38]. Finally, the presence of current-driven magnetic anisotropy, Eq. (1), is expected to add new functionalities to Fe_3GeTe_2 and its interplay with the perpendicular DMI reported in the present communication remains to be investigated in details.

ACKNOWLEDGMENTS

S.L. and A.M. thank G. Bihlmayer, S. Blügel and A. T. Costa for useful discussions. This work was supported by the King Abdullah University of Science and Technology (KAUST) through the Office of Sponsored Research (OSR) [Grant Number OSR-2017-CRG6-3390]. K.-W. K acknowledges support from the KIST institutional program and the National Research Council of Science & Technology (NST) (CAP-16-01-KIST).

* slimane.laref@kaust.edu.sa
† aurelien.manchon@kaust.edu.sa

[1] Huang et al., Nature **546**, 270 (2017).
[2] Li et al., Advanced Materials **30**, 1801043 (2018).
[3] Sun et al., arXiV:1909.09797v1 (2019).
[4] Deng et al., Nature **563**, 94 (2018).
[5] Zhang et al., Applied Physics Letters **116**, 042402 (2020).
[6] Park et al., Nano Letters **20**, 95 (2020).
[7] Alghamdi et al., Nano Letters **19**, 4400 (2019).
[8] X. Wang, J. Tang, X. Xia, C. He, J. Zhang, and Y. Liu, Science Advances **5**, eaaw8904 (2019).
[9] J. Xu, W. A. Phelan, and C.-l. Chien, Nano Letters **19**, 8250 (2019).
[10] Fang et al., Applied Physics Letters **115**, 212402 (2019).
[11] Z. Wang, D. Sapkota, T. Taniguchi, K. Watanabe, D. Mandrus, and A. F. Morpurgo, Nano Letters **18**, 4303 (2018).
[12] Albarakati et al., Science Advances **5**, eaaw0409 (2019).
[13] Wang et al., arXiv:1907.08382 (2019).
[14] Ding et al., arXiv:1912.11228 (2019).
[15] Park et al., arXiv:1907.01425 (2019).
[16] I. Dzyaloshinskii, Soviet Physics JETP **5**, 1259 (1957).
[17] T. Moriya, Physical Review **120**, 91 (1960).
[18] N. Nagaosa and Y. Tokura, Nature nanotechnology **8**, 899 (2013).
[19] G. Chen, A. Mascaraque, A. T. N?Diaye, and A. K. Schmid, Applied Physics Letters **106**, 242404 (2015).
[20] O. Johansen, V. Risinggard, A. Sudbo, J. Linder, and A. Brataas, Physical Review Letters **122**, 217203 (2019).
[21] F. Freimuth,S. Blügel, and Y. Mokrousov, Journal of Physics: Condensed Matter **26**, 104202 (2014).
[22] Zelezny et al., Physical Review B **95**, 014403 (2017).
[23] A. Raeliarijaona, R. Nepal and A. A. Kovalev, Physical Review Materials **2**, 124401 (2018).
[24] K. M. D. Hals and K. Everschor-Sitte, Physical Review Letters **119**, 127203 (2017).
[25] S. Rohart and A. Thiaville, Physical Review B **88**, 184422 (2013).
[26] You et al., Physical Review B **100**, 134441 (2019).
[27] http://www.flapw.de
[28] P. Kurz, F. Förster, L. Nordström, G. Bihlmayer, and S. Blügel, Physical Review B **69**, 024415 (2004).
[29] M. Heide, G. Bihlmayer, and S. Blügel, Physica B: Condensed Matter **404**, 2678 (2009).
[30] Ferriani et al., Physical Review Letters **101**, 027201 (2008).
[31] A. Belabbes, G. Bihlmayer, F. Bechstedt, S. Blügel, and A. Manchon, Physical Review Letters **117**, 247202 (2016).
[32] J. P. Perdew, K. Burke, and M. Ernzerhof, Physical Review Letters **77**, 3865 (1996).
[33] J. P. Perdew and A. Zunger, Physical Review B **23**, 5048 (1981).
[34] A. Belabbes, G. Bihlmayer, S. Blügel, and A. Manchon, Scientific Reports **6**, 24634 (2016).
[35] Kashid et al., Physical Review B **90**, 054412 (2014).
[36] Jeongwoo Kim, Kyoung-Whan Kim, Bumseop Kim, Chang-Jong Kang, Dongbin Shin, Sang-Hoon Lee, Byoung-Chul Min, and Noejung Park, Nano Letters **20**, 929 (2020).
[37] Congkuan Tian, Feihao Pan, Sheng Xu, Kun Ai, Tianlong Xia, and Peng Cheng, Applied Physics Letters **116**, 202402 (2020).
[38] Yun-Peng Wang, Xiao-Yan Chen, and Meng-Qiu Long, Applied Physics Letters **116**, 092404 (2020).